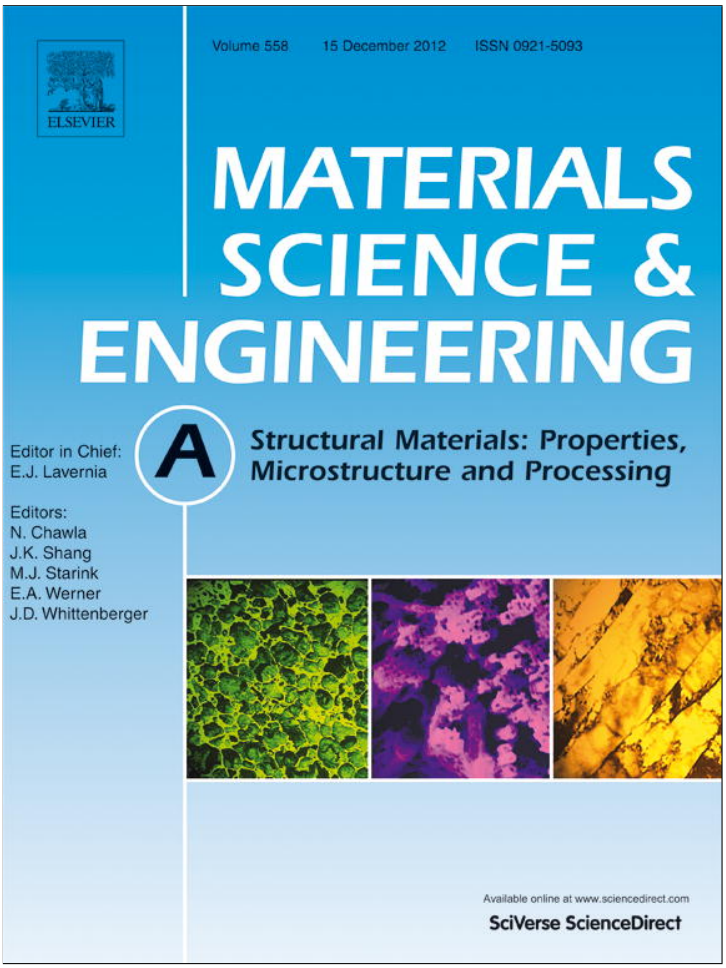

Materials Science & Engineering A 558 (2012) 21–29

Contents lists available at SciVerse ScienceDirect

Materials Science & Engineering A

journal homepage: www.elsevier.com/locate/msea

Mechanical properties, modeling and design of porous clay ceramics

I. Yakub [a,b], J. Du [a,b], W.O. Soboyejo [a,b,*]

[a] Princeton Institute of Science and Technology of Materials (PRISM), Princeton University, 70 Prospect Street, Princeton, NJ 08540, USA
[b] Department of Mechanical and Aerospace Engineering, Princeton University, Olden Street, Princeton, NJ 08544, USA

ARTICLE INFO

Article history:
Received 19 January 2012
Received in revised form
23 May 2012
Accepted 10 July 2012
Available online 7 August 2012

Keywords:
Porous clay ceramics
Mechanical properties
Strength
Fracture toughness
Resistance-curve behavior
Finite element analysis

ABSTRACT

Porous ceramics with three different porosities were fabricated by the sintering of redart clay and woodchips (sawdust). The latter was used as the pore-forming agent in porous ceramic water. The porosity, pore size and density of the materials were characterized using Mercury Intrusion Porosimetry and Helium Pyncnometer technique, while the structure and chemistry of the materials were elucidated via X-ray diffraction (XRD), environmental scanning electron microscopy (ESEM) and energy dispersive X-ray spectroscopy (EDX). The compressive strength of the porous clay ceramics were found to exhibit a downward trend with increasing porosity. Due to the anisotropic nature of the porous material, two types of specimen (T- and S-Type) were fabricated for the measurement of flexural strength, fracture toughness and resistance-curve behavior under three point bending. The observed crack-tip shielding/toughening mechanism was then modeled using fracture mechanics concepts. The measured mechanical/physical properties, such as: elastic modulus, density and porosity, were then incorporated into finite element models for the computation of stress distributions due to hydrostatic pressures exerted on the porous clay ceramics by the water in filter with different geometries and supporting configurations. The implications of the results are discussed for potential scale-up and design of a mechanically robust porous ceramic for water filtration.

1. Introduction

Porous ceramics are a class of materials that cover a wide range of structures including (but not limited to): foams, honeycombs, interconnected rods, interconnected fibers and interconnected hollow spheres [1]. The properties of porous ceramics such as density, surface area, permeability, porosity, hardness, modulus, wear resistance, corrosion resistant and thermal conductivity, may be controlled by controlling their structure and nature. This has ultimately led to porous ceramics having a wide range of applications, which include prosthetics and biomedical devices; electronic sensors; refractory materials (thermal insulators); heat exchangers; bioreactors; and for separating materials in food, chemical and pharmaceutical industry [2,3]. They are also used in environmental technologies (e.g. the catalytic converter). A promising application of porous clay-based ceramic is in their use in water purification [4–7].

About 884 million people worldwide lack access to improved water supplies and as a result approximately 1.5 million people, mostly children, die every year [8]. The ceramic water filter (CWFs) is one of the few types of point-of-use (POU) water purification system that is currently been used to tackle this scourge. CWFs are fabricated by mixing clay with a combustible or pore forming material (usually sawdust, flour and rice husk) with a binder (water). The resulting homogenous mixture is then pressed using a mechanical press, or in some cases by manual molding using pottery wheel, into the desired shaped. The frustum (or pot) shape is the most popular shape. However, other filter geometries do exist, such as disk shapes and candle shapes [9,10]. During sintering, the combustible material burns off and leaves behind pores. The micro- and nano-scale pores form complicated porous network. The geometry and surface properties of the pores are also the primary keys to the CWFs successful removal of microbial contaminants to levels that are below the WHO standard [11,12]. CWFs can also reduce the turbidity of water to the acceptable levels provided it is designed, used and maintained properly [13,14].

Furthermore, the clay–water mixture is a combination that can be doped with other materials. This affords the CWFs the robustness required for the removal of other contaminants besides microbial contaminants from water. The removal of chemical contaminants such as arsenic, iron and fluorine has been reported [14–16]. Moreover, it has also been shown that with the right amount of iron oxide doping, the CWFs are capable of removing viruses [17,18].

* Corresponding author at: Princeton Institute of Science and Technology of Materials (PRISM), Princeton University, 70 Prospect Street, Princeton, NJ 08540, USA. Tel.: +1 609 258 5609; fax: +1 609 258 5877.
E-mail address: soboyejo@princeton.edu (W.O. Soboyejo).

0921-5093/$ - see front matter © 2012 Elsevier B.V. All rights reserved.
http://dx.doi.org/10.1016/j.msea.2012.07.038

The porous nature of the CWFs makes them susceptible to failure. This leads to filter breakage during processing, distribution (transportation) and usage. The latter is because the filter has to be able to support its own weight on its lips (which rests on the rim of a receptacle) during operation (due to the hydrostatic pressure of water). There is, therefore, a need to relate the mechanical properties of the porous clay ceramics to their porosity and pore size distributions. There is also a need to fabricate filters with improved structural integrity. This can be achieved by re-designing the filter geometries and by finding ways to toughen them.

In this paper, clay ceramics with three different levels of porosity were produced by the sintering of clay/sawdust mixture with ratios of 50:50, 65:35 and 75:25 by volume. The structure and mechanical properties (elastic modulus, hardness, compressive strength, flexural strength, fracture toughness and resistance-curve behavior) were studied using a combination of experiments and models. The finite element method (FEM) was then used to study the stress distributions due to the hydrostatic pressures exerted on the filter walls with different shapes and support configurations. The implications of the results are then discussed for the scale up of ceramic water filtration and the design of filter shapes and structures with improved robustness.

2. Experimental

2.1. Materials and processing

The (redart) clay that was used in this study was obtained from Cedar Heights (Cedar Heights Redart Airfloated Clay, Pittsburgh, PA). The chemical composition of the clay is given in Table 1. The sawdust (woodchips) used was obtained from a local sawmill (Hamilton Building Supplies, Trenton, NJ). The clay was mixed with the sawdust in three different ratios (clay-to-sawdust) by volume, viz 50:50 (or 50–50), 65:35 (or 65–35) and 75:25 (or 75–25). Prior to mixing, the sawdust was manually sieved using 35–1000 mesh wire sieves. The clay was then blended with sawdust in an industrial mixer (Model A-200, The Hobart Manufacturing Company, Troy, OH), with water as the binding agent.

The resulting mixture (clay, sawdust and water) was formed into a dough shape (about 5.5 kg/12 lbs is required to make a CWFs). The dough was then formed into a frustum-shape, with a two-piece frustum-shaped aluminum mold. This was done using a 50 t hydraulic press (TRD55002, Torin Jacks, Inc., Ontario, Canada). The resulting greenware was dried in laboratory air (temperature of 25 °C, humidity of 40%) for about 5–8 days. After drying, the greenware was sintered in a gas kiln (Ceramics Art Department, Princeton University, Princeton, NJ). The firing involved pre-heating of the greenware to 450–550 °C for three hours (to burn off the sawdust), followed by heating to the sintering temperature of 955 °C in the same gas kiln. The initial heating rate of 50 °C per hour was increased to 100 °C per hour beyond a furnace temperature of 200 °C. The CWFs were sintered for 5 hours at the peak temperature of about 955 °C. They were then furnace-cooled in air to room-temperature.

The frustum-shaped CWFs consists of two sections, the base (or disk part) and the side (or curved part). The disk has a radius of ~91.5 mm and a thickness of ~15 mm. The side has a slant height of ~240 mm and is ~10 mm thick. The CWFs is ~237 mm deep, and hence has a capacity of about 10 L. In this study, only the base (or disk part) of the CWFs was used in the characterization of the structure and mechanical properties of the porous clays ceramics. The sides were not used due to their curvature.

Table 1
Chemical composition of redart clay raw material.

Component	SiO_2	Al_2O_3	Fe_2O_3	TiO_2	MgO	CaO	Na_2O	K_2O	Other	LOI*
Fraction (wt%)	64.2	16.4	7	1.1	1.6	0.2	0.4	4.1	0.1	4.9

* LOI = Loss on ignition.

2.2. Materials characterization

The porosities, (average) pore-size, bulk density and skeletal density of the porous clay ceramics were measured using a Mercury Porosimeter [19]. The porosimetry measurements were carried out in a MicroMetrics Autopore III 9400 analyzer (MicroMetrics, Norcross, GA). The two-stage MP experiments were performed on pieces with dimensions of ~3 mm × 3 mm × 3 mm that were cut from the three different porous ceramics (50:50, 65:35 and 75:25). The skeletal density of the porous ceramic was also found using a AccuPyc 1330 Helium Pyncometer (HP) (MicroMetrics, Norcross, GA).

The surface morphology of the woodchips and the three porous ceramic was carried out using the Environmental Scanning Electron Microscope (ESEM) (Quanta 200 FE-ESEM, FEI, Hillboro, OR). The elements present in the redart clay and porous clay ceramics were also verified using the Oxford EDX detector (Oxford Instruments, Oxfordshire, UK) on the Environmental SEM. X-ray diffraction (XRD) was performed on powders of redart clay and porous clay ceramics to determine their phase compositions. This was done using a Bruker D8 Advance diffractometer, with secondary graphite monochoromator and Cu-Kα radiation (λ=0.15418 nm). The scan step was 0.02° and the step time was 0.8 s per step. The measurement was done over the interval $10^\circ < 2\theta < 70^\circ$. The entire operation was carried out at room temperature (25 °C).

2.3. Modulus and hardness measurement

Nanoindentation was used to obtain the moduli and hardness values of the porous ceramic. The indentation studies were performed in a TriboScope nanomechanical testing system (Hysitron Inc., Minneapolis, MN), coupled to a Dimension 3100 scanning probe microscope (Veeco Instruments Inc., Woodbury, NY). A three-plate capacitive transducer was used by the TriboScope to control the applied load. A conical (spherical-tipped) indenter with a norminal tip radius of ~100 μm was used. The loading profile consisted of the following three steps: loading at a rate of 5 μN/s to a peak load of 1000 μN; holding at the peak load for 5 s, and returning to zero load at an unloading rate of 5 μN/s. For each porous ceramic type, 45 nanoindentation measurements were obtained.

2.4. Strength measurements

Both the compressive strength and flexural strength testing were carried out in an Instron Model 8872 servo-hydraulic testing machine (Instron, Canton, MA) instrumented with a load cell of 25 kN. The compressive strengths of the porous clay ceramics were obtained by compressive loading of bars of height, H=35 mm, width, W=12.63 mm, and breadth, B=12.63 mm was used. These were loaded to failure at a rate of 0.1 N s^{-1}. The compressive strength was then evaluated from the following expression:

$$\sigma_c = \frac{P}{BW} \tag{1}$$

where P is the load at failure; B and W are the respective breadth and width of the rectangular specimens.

The flexural strengths or moduli of rupture [20] were obtained by the bend testing of bars of height, H, of 12.63 mm, width, W, of 12.63 mm, and length, L, of 76 mm. Two types of specimens were made due to the anisotropic nature of the porous clay ceramics. The specimens were oriented for fracture in the short transverse and traverse orientations, referred to here as "S-Type" and "T-Type" specimen respectively. The bend testing was done under three-point bend loading at a cross-head speed of 0.1 N s^{-1} and a loading span of 40 mm.

The MOR was then evaluated from the following expression [21]:

$$MOR(\sigma) = \frac{3PS}{2B^2W} \tag{2}$$

where S is the loading span, P is the applied load at the onset of failure, while the other constants have their usual meanings.

2.5. Fracture toughness

Due to the anisotropic nature of the porous clay ceramics, fracture toughness (K_{Ic}) tests were performed on two types of single-edge notched-bend (SENB) specimens. The specimens mainly differ by the orientation of the notch. Specimens with height, H, of 12.63 mm, width, W, of 12.63 mm, and length, L, of 76 mm, were used. The specimens were tested using the Instron 5848 MicroTester (Instron, Canton, MA) instrumented with a 500 N load cell. The specimens were loaded monotonically to failure at a loading rate of 0.1 N s^{-1}, with a loading span of 35 mm. An initial notch, with a notch-to-width ratio (a/W) of ~0.25, was introduced at the center of the specimens. Fracture toughness, K_{Ic}, was determined from the following expression [22,23]:

$$K_{Ic} = \frac{PS}{BW^{3/2}} \times f\left(\frac{a}{W}\right) \tag{3}$$

where a is the crack length (depth of the notch), $f(a/W)$ is the compliance function and the other constants have their usual meaning.

2.6. Resistance-curve measurements

Resistance-curve experiments were also performed on the same type of SENB specimens that were used in the fracture toughness measurements. The experiments were performed under three-point bend loading. Crack growth was monitored with Krak gages (KG-A05, Hartrun Corp., Eden Prairie, MI) bonded to the specimen surfaces with the Epotek 353ND (Epoxy Technologies Inc., Billerica, MA). After curing for 24 h, four wires were soldered on to the Krak gage and connected to a FRACTOMAT system (Model 1288, Hartrun Corp., Eden Prairie, MI), which is a two-channel microprocessor-based instrument for monitoring crack growth. The FRACTOMAT system was connected to a NI CB-68LP board (National Instrument, Austin, TX) that was linked to a computer with LABView software package (National Instruments, Austin, TX). The latter was used to collect the voltage data (due to crack growth) as a function of time. The specimens were loaded in incremental steps to peak loads below the critical loads. The loads were then increased in incremental steps, while the corresponding incremental crack growths were monitored using the *in-situ* Krak gages. This was continued until the crack growth reached the steady-state regime. In this way, the resistance curves were obtained for all the porous ceramics.

3. Modeling

3.1. Crack-tip shielding

The resistance of the porous ceramic to crack growth was quantified in this section using a combination of small- and large-scale crack bridging models. For small scale bridging, where it is assumed that the bridging zone is small compared to the crack size ($\Delta a < 0.5$ mm), the toughening due to small to small-scale crack bridging, ΔK_{ssb}, is given by

$$\Delta K_{ssb} = \sqrt{\frac{2}{\pi}} \int_0^{l_B} \alpha V_B \frac{\sigma(x)}{\sqrt{x}} dx \tag{4}$$

where l_B is the bridge length (which is equal to the distance from the crack-tip to the last unfractured reinforcement), $\sigma(x)$ represents the bridging traction across the ductile reinforcement, x is the distance from the crack face behind the crack-tip, α is the triaxiality/constraint factor [24], and V_B is the volume fraction of the ligaments.

In the case where the bridging zone is comparable to the overall crack dimensions ($\Delta a \geq 0.5$ mm), large scale bridging models are used to estimate the shielding contributions from crack bridging. The shielding due to large-scale bridging, ΔK_{lsb}, is given by [25,26]:

$$\Delta K_{lsb} = \int_0^L \alpha V_B \sigma(x) h(a,x) dx \tag{5}$$

where L is the length of the bridging zone, α is the constraint/triaxiality factor, V_b is the volume fraction of bridging ligaments, $\sigma(x)$ is traction function along the bridge zone, and $h(a,x)$ is a weighting function given by Fett and Munz [27].

The overall resistance curve behavior may be estimated by the application of the principle of linear superposition. This gives:

$$K_{app} = K_{tip} + \Delta K \tag{6}$$

where K_{app} is the applied stress intensity factor, K_{tip} is the initiation toughness and ΔK is the toughening due to small-scale crack bridging ($\Delta a < 0.5$ mm) or large-scale bridging ($\Delta a \geq 0.5$ mm) as the case may be.

3.2. Finite element analysis

The objective of Finite Element Analysis (FEA) is to optimize the geometry and supporting configuration of the water filters under the effects of hydrostatic pressure. The finite element software ABAQUS™ v6.9-EF2 (ABAQUS, Inc., Pawtucket, RI) was used in the study. Axisymmetric finite element models of filters were developed as shown in Fig. 1. A 4-node linear axisymmetric element was used. The mesh was refined at the corners as in Fig. 1(a). The diameter, thickness, height and angle of the frustum model (Fig. 1(a)) are the same as that of typical CWFs, as described in Section 4.2.

Figs. 2(a)–(g) shows the different support configuration that was used in the modeling of the frustum-shaped filter. Models of potential uniform thickness filter model, ellipsoidal filter model, semi-spherical filter model, cylindrical filter model, and inverted frustum filter model, were also built, as shown in Fig. 1(b)–(e), respectively. The same wall thicknesses and heights were used in all the filter models.

The measured mechanical properties of the 65–35 filter, such as Young's modulus, density and porosity, were used for this study (Table 2 and Table 3). It was assumed that all the materials exhibited isotropic elastic behavior. The axisymmetric boundary condition was also applied at the symmetry axis. The bottoms of the filter lips were fixed to have no displacements or rotations. A hydrostatic pressure load was applied on the inner surface of each

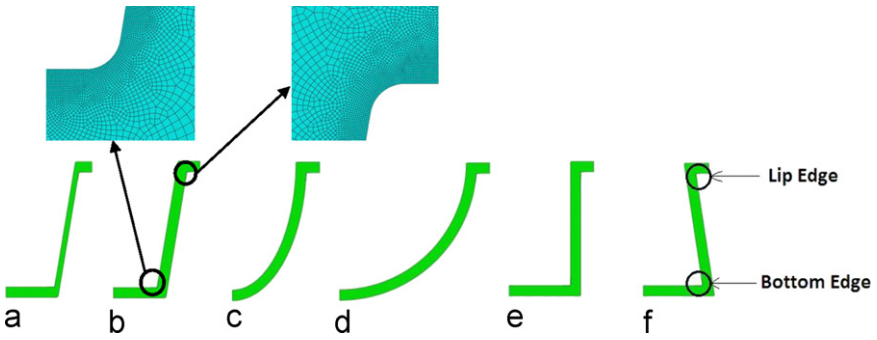

Fig. 1. Finite element axisymmetric models of the filters for (a) frustum filter model, (b) uniform thickness frustum filter model, (c) ellipsoid filter model, (d) semi-spherical filter model, (e) cylindrical filter model, and (f) inverted frustum filter model.

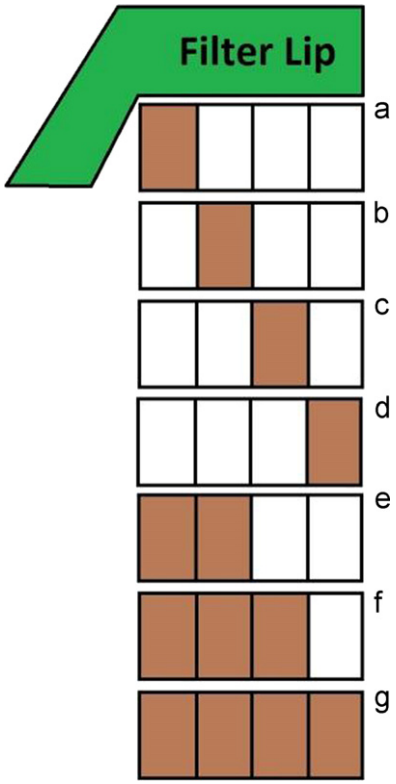

Fig. 2. Different support configurations modeled. Figure shows support spanning (a) 1st quarter of lip, (b) 2nd quarter of lip, (c) 3rd quarter of lip, (d) 4th quarter of lip, (e) 1/2 of lip, (f) 3/4 of lip and (g) the entire lip.

filter to simulate the effects of water in the filter. In this way, the stress distributions were computed for the possible filter designs. A body force was applied on each filter to simulate the effects of the filter self-weight and the weight of water contained within the filter during operation. In this way, the stress distributions were computed for the different filter designs.

4. Results and discussion

4.1. Materials characterization

Fig. 3(a) is the environmental scanning electron micrograph of the woodchips (sawdust) used in making the porous ceramics. Micrographs of the surface of the three different porous clay ceramic studied are given in Fig. 3(b)–(d). The micrographs reveal the presence of microscopic pores. The bulk density and skeletal density (using HP and MP) are found to increase with increasing sawdust content (Table 2). One hypothesis is that the greenware with higher sawdust content, burns off quicker than a greenware with lower sawdust content. This is because of larger pathways/channels available expulsion of the combustion products (mainly carbon dioxide). As a result, the greenware with the higher sawdust content has more time to sinter (due to the relatively early eviction of the sawdust).

Furthermore, the skeletal density measured by the helium pycnometer (HP) was greater than that measured by the mercury porosimeter [19]. This suggests that the porous ceramic had pore sizes below the detectable limits of the MP method. This higher skeletal density measured by the HP resulted in a higher porosity, compared with the values for MP (Table 2). This is because of helium gas has a small atomic radius (~31 pm) and is thus able to seep through pico-scale pores. The mercury porosimetry on the other hand is only effective for pores diameter greater 3 nm. The linear relation between the two types of porosities is shown in Fig. 4. This exhibits a correlation coefficient, R^2, of about 0.995. Both the MP and HP porosities were found to increase with increasing sawdust content (that was used in fabricating the porous ceramic). No apparent trends were observed between the measured porosities and the average pore sizes (Table 2). The firing of the CWFs is sometimes carried out under controlled conditions that result in carbon residues from the sawdust. However, the EDX analysis revealed no trace of carbon, meaning all of the sawdust was completely burnt off during the firing process (See supporting information S1). Also, the EDX is a necessary prerequisite to X-ray diffraction. The X-ray diffraction analyses of the redart clay and the porous ceramics are presented in Fig. 5. The results show that the redart clay and porous ceramic exhibit similar diffraction patterns. The redart clay structure consists predominantly of illite and kaolinite mineral. Above 500 °C, the kaolinite mineral (which has a weight percent of about 10%) undergoes an endothermic dehydroxylation process. This transforms it into a disordered alumino-silicate, metakaolinite [21,28]. The kaolin clay, which was originally crystalline, is now transformed into metakaolin,which is amorphous. This explains the shorter peaks in the porous ceramics, and why some of the peaks (that existed in the redart clay) are missing in the porous ceramics.

4.2. Modulus and hardness

Elastic modulus and hardness are not strictly functions of porosity but also depend on pore morphology, pore size distribution (and arrangement) and microstructure [29–32]. The unrelaxed moduli and hardnesses of the porous ceramics, indented using a spherical (conical) indenter, are plotted as a function of porosity and average pore size in Fig. 6(a) and (b). The results showed that the modulus and hardness do not have any clear

Table 2
Physical properties of porous ceramic. MP is Mercury Porosimeter and HP is Helium Pyncnometer.

Porous ceramic type	Volume fraction of sawdust (%)	Average pore diameter (μm)	Bulk density (g/cm^3)	Skeletal density (g/cm^3)		Porosity (%)	
				MP	HP	MP	HP
75–25	25	0.605	1.500	2.358	2.720	36.384	44.848
65–35	35	0.551	1.424	2.411	2.731	40.891	47.854
50–50	50	1.074	1.286	2.424	2.741	46.955	53.095

Table 3
Summary of mechanical properties of the porous ceramics.

Porous ceramic type	Volume fraction of sawdust (%)	Porosity (%)	Average pore diameter (μm)	Compressive strength (MPa)	Young's modulus (GPa)	Hardness (MPa)	Specimen type	MOR (MPa)	Fracture toughness, K_{Ic} (MPa. m$^{0.5}$)
75–25	25	36.38	0.605	9.11 ± 0.47	1.66 ± 0.44	22.93 ± 9.66	T	5.39 ± 1.72	0.61 ± 0.03
							S	7.16 ± 2.26	0.47 ± 0.09
65–35	35	40.89	0.551	7.41 ± 0.84	3.06 ± 0.73	39.15 ± 12.72	T	4.22 ± 0.12	0.40 ± 0.05
							S	4.64 ± 1.16	0.43 ± 0.03
50–50	50	46.96	1.074	5.25 ± 0.19	1.36 ± 0.20	20.36 ± 8.94	T	3.89 ± 0.09	0.35 ± 0.02
							S	4.29 ± 0.53	0.37 ± 0.02

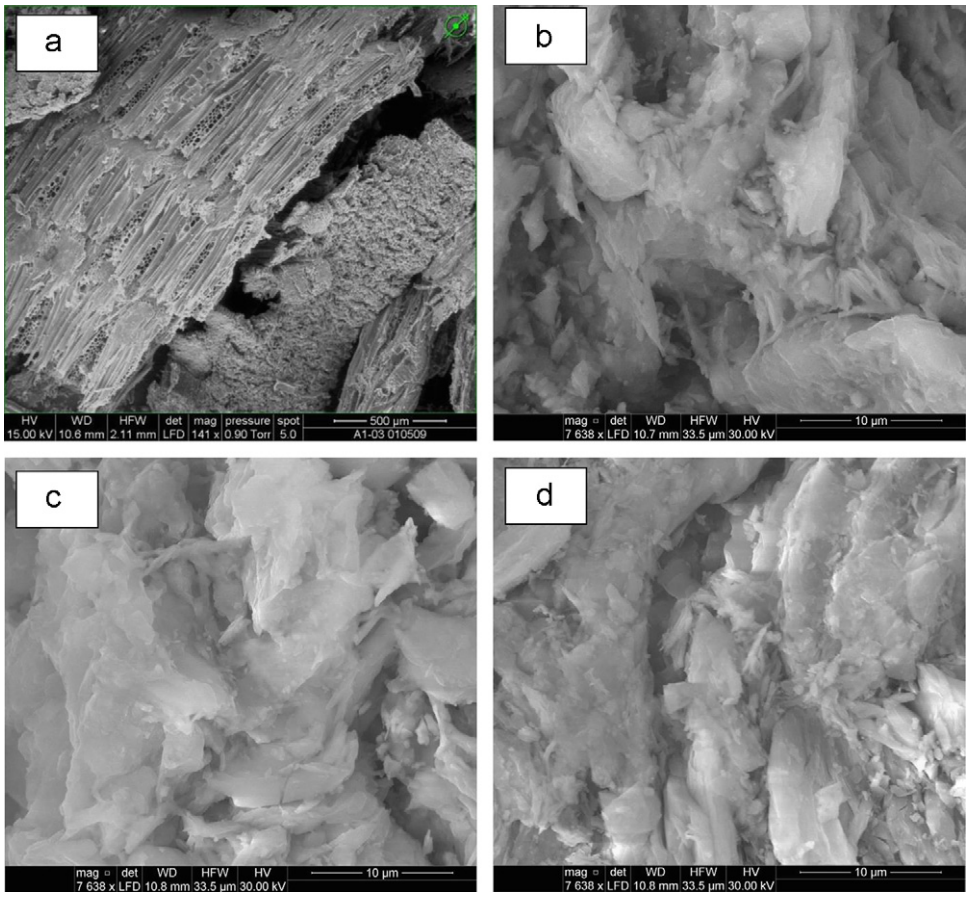

Fig. 3. Environmental scanning electron microscopy micrographs of (a) the woodchips (sawdust) used, (b) 50:50 porous ceramic, (c) 65:35 porous ceramic and (d) 75:25 porous ceramic.

relationship with porosity but increased as the average pore size is decreased.

4.3. Compressive and flexural strength

The compressive strengths decreased linearly (R^2=0.9997) with increasing porosity (Fig. 7). A better fit can be obtained considering a wider range of porosities, the problem however is that making filters below porosity of ~35% significantly decreases the flow rate of CWFs and porosity above ~50% significantly reduces the strength of the filter and may drastically reduce its microbial efficacy. The flexural strength [20] of the porous ceramic is also seen to decrease with decreasing porosity (Fig. 8). Similar trends have been observed by other researchers [30,33,34]. It was also observed that the MORs of the "S-Type" specimen were somewhat greater than those of the "T-Type"

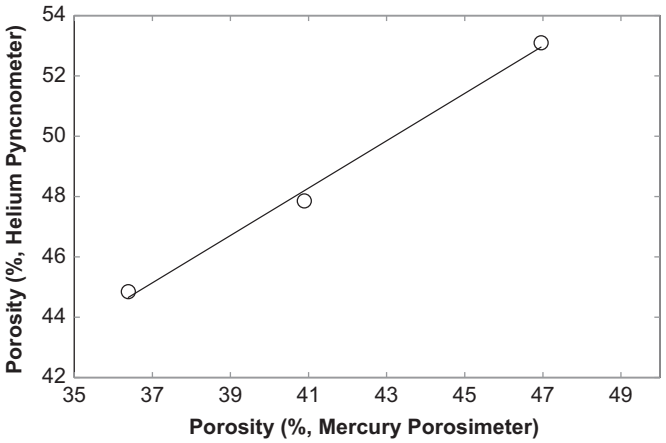

Fig. 4. Linear relationship between porosity measured using helium pycnometer and mercury porosimeter.

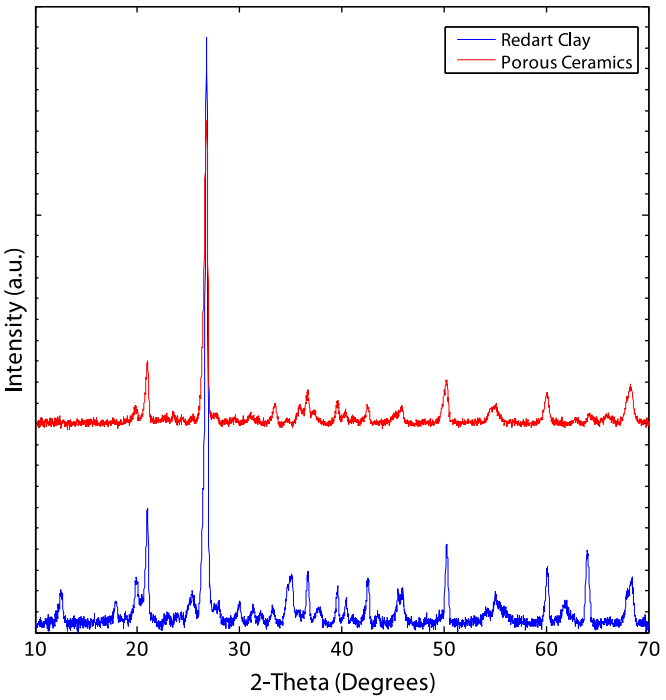

Fig. 5. XRD pattern of Redart clay (bottom/blue) and the porous ceramic (top/red). (For interpretation of the references to color in this figure legend, the reader is referred to the web version of this article.)

specimens. This is because the flexural strength largely depends on surface condition and the "S-Type" surface is relatively denser compared to the "T-Type" due to nature of sintering. Both the compressive and flexural strengths are generally attributed to stress concentration phenomena [35–37].

4.4. Fracture toughness and resistance-curve behavior

The fracture toughness (of both specimen types) decreases with increasing porosity (Fig. 9). Similar trends have been reported by other researchers [32]. The fracture toughness for the "T-Type" specimen fell sharply for porosities of ~36% and ~41%. This may be due to a reduction in crack deflection and the critical strain energy release rate. At $\Phi = 40.3\%$, the porous ceramic material becomes isotropic with respect to fracture toughness. The resistance-curve behavior of the ceramic obtained using the Krak gage is given in Fig. 10. The result shows that the

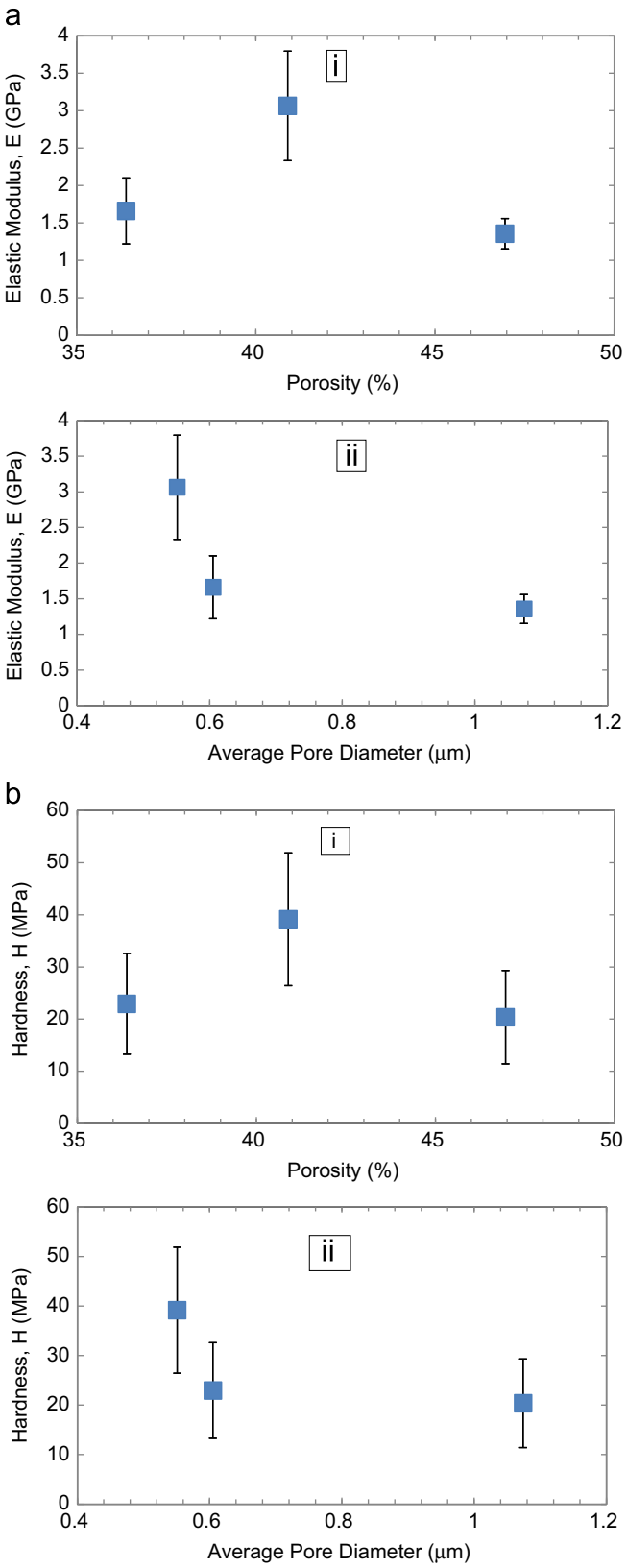

Fig. 6. Variation of elastic modulus and hardness with porosity and average pore diameter. (a) Variation of elastic modulus with (i) porosity and (ii) average pore diameter. (b) Variation of elastic modulus with (i) porosity and (ii) average pore diameter.

porous ceramic exhibited very limited crack growth resistance, as is typical of brittle materials. The limited crack growth resistance

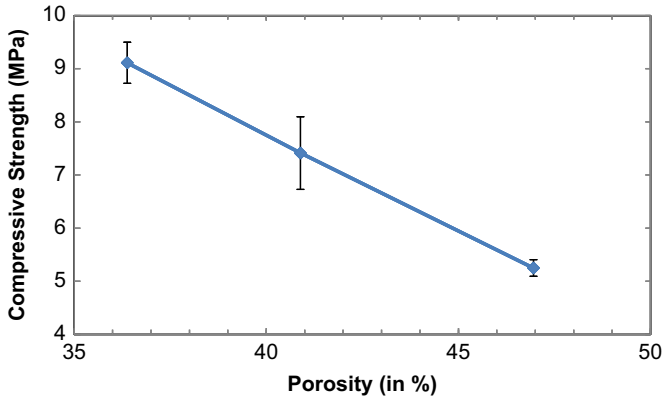

Fig. 7. Dependence of compressive strength on porosity of the porous ceramics.

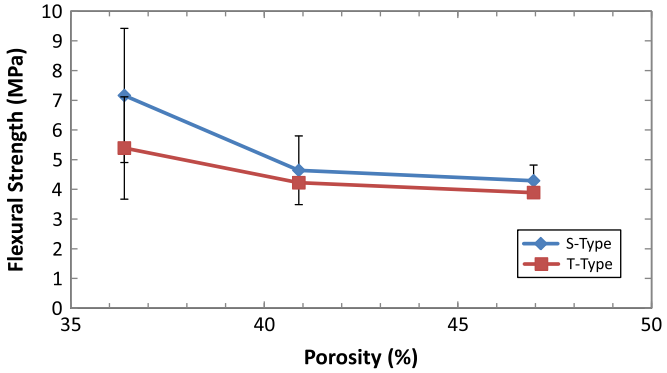

Fig. 8. Dependence of flexural strength on porosity of the porous ceramics.

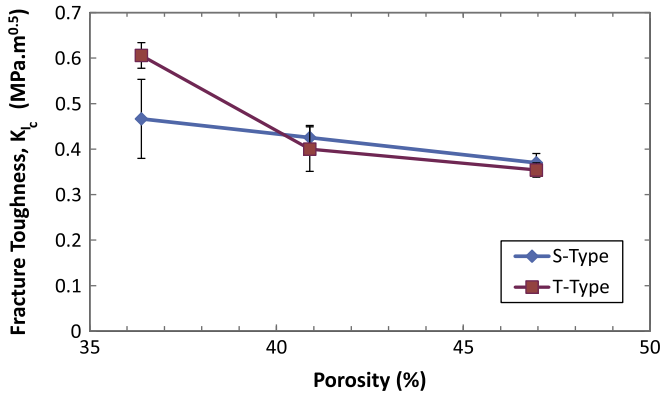

Fig. 9. Dependence of fracture toughness on porosity of the porous ceramic.

was attributed largely to crack bridging. Evidence of crack-tip shielding by crack bridging is presented in Fig. 11.

4.5. Modeling of filter stress

4.5.1. Effects of supporting configurations

Table 4 shows the maximum principal stress at the lip edge and bottom edge for the filter under two extreme conditions: when dry and when filled with water. Also shown in the table is the variation of maximum principal stress with different support conditions. It is seen that the maximum principal stress at the bottom edge (for both the dry and filled filter) has a weak dependence on the support configuration. This may be because

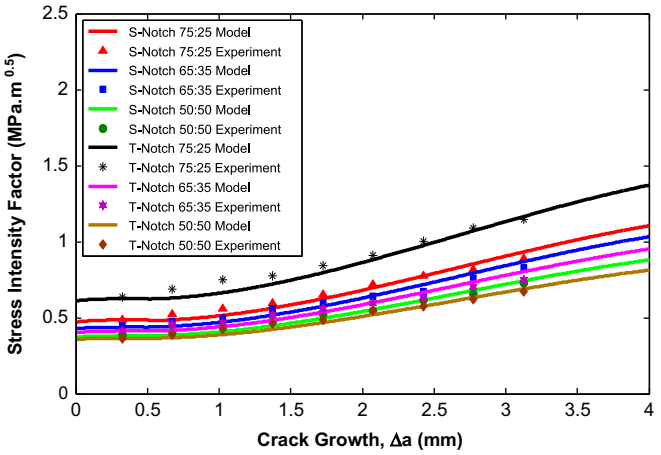

Fig. 10. Resistance curve behavior of the porous ceramic.

the bottom edge is far away from the filter lip which is being supported. For the dry filter, for any given support system the maximum principal stress at the lip edge was generally greater than the maximum principal stress at the bottom edge. The reverse is true for the filter when it is filled with water. This is because when the filter is dry, i.e. during storage and transportation, the lip undergoes greater stress than the bottom. Also, when water is added to the filter, it increases the bending moment on the bottom section, by a lot, and makes it much larger than that in the lip. This indicates that the filter is more likely to fail at the lip when it is dry. It is also more likely to fail at the bottom, when it is wet, i.e. during use.

Fig. 12 shows the maximum principal stress as a function of hydrodynamic head of the water (measured from the base of the filter up). This mimics the change in maximum principal stress as the filter is drained. The graph also shows the variation of the maximum principal stress with support configuration. For any support configuration, the maximum principal stress at the bottom edge is more or less the same as shown by the dash line in Fig. 12. From both Fig. 12 and Table 4, it is apparent that the closer the support is to the (side of the) filter, the lower the stress at its lip edge. This is because closer support gives a smaller bending moment to the lip. The worst scenario is when the support was at the "fourth quarter". Not only does it have the highest maximum principal stress at any given pressure head, it has the longest range of maximum principal stress per cycle. A cycle is defined as the time it takes a filter that is completely filled with water to empty out its content. Also, the best support configuration is the one that spans the entire lip of the filter. In this case the applied bending moment is minimized.

4.5.2. Effects of filter geometries

Fig. 13 shows the maximum principal stress as a function of hydrodynamic head of the water. The modeling was carried out with support fully spanning the entire lip. For reasons mentioned in Section 4.5.1, for any given filter model (and for the same pressure head) the maximum principal stress on the filter lip is generally greater than that at the bottom of the filter. Fig. 13 also shows that the uniform frustum shaped model is better than the regular frustum shaped filter. This is because it has a higher second moment of area (due to higher thickness). In terms of stresses on the filter bottom edge, the general order (from best to worst) is as follows: ellipsoidal model > semi-spherical model > uniform thickness frustum shaped model > frustum shaped model > inverted frustum model > cylindrical model. Ellipsoidal and semi-spherical filters have lower stress concentration

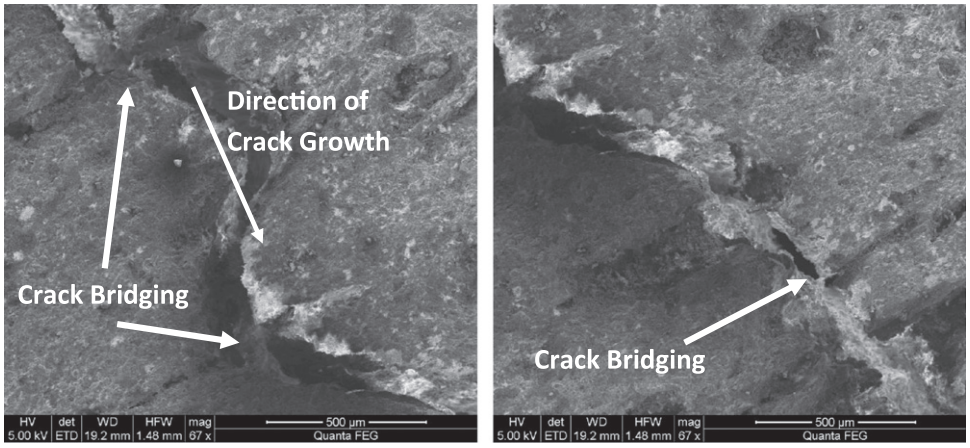

Fig. 11. ESEM image of a porous ceramic showing evidence of crack bridging.

Table 4
Maximum principal stress (in MPa) in the "lip edge" and "bottom edge" of the frustum-shaped filter under different support condition.

Support condition	Dry		Filled to the brim with water	
	Lip edge	Bottom edge	Lip edge	Bottom edge
1st quarter of lip	0.0221765	0.0148261	0.0926826	0.162217
2nd quarter of lip	0.0253766	0.0148275	0.101166	0.162222
3rd quarter of lip	0.0328176	0.0148293	0.12904	0.162228
4th quarter of lip	0.0447144	0.014832	0.175444	0.162239
1st quarter of lip	0.0221765	0.0148261	0.0926826	0.162217
1/2 of lip	0.0185462	0.0148254	0.0712261	0.162213
3/4 of lip	0.0165832	0.0148251	0.0611436	0.162211
The entire lip	0.0157076	0.014825	0.056979	0.16221

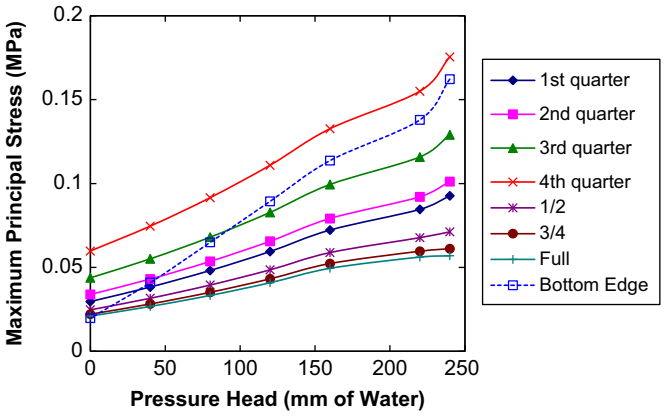

Fig. 12. Variation of the maximum principal stress on the "lip edge" and the "bottom edge" of the frustum-shaped filter as the pressure head of water changes.

because of the roundness its bottom edge. Uniform thickness frustum filter has thicker wall than the frustum filter, and therefore have a greater stiffness. The cylindrical filter appears to be the worst because of effects of bending moments. In terms of stresses on the filter lip edge, the order (from best to worse) is as follows: frustum shaped model > ellipsoidal model > uniform thickness frustum shaped model > cylindrical model > inverted frustum model. This is largely because of effect of bending moments due to a combination of filter self-weight and hydrostatic pressure. It is hard to rank the semi-spherical model. It appears to be better at handling stress at lower pressure head and worse at handling stress at higher pressure head.

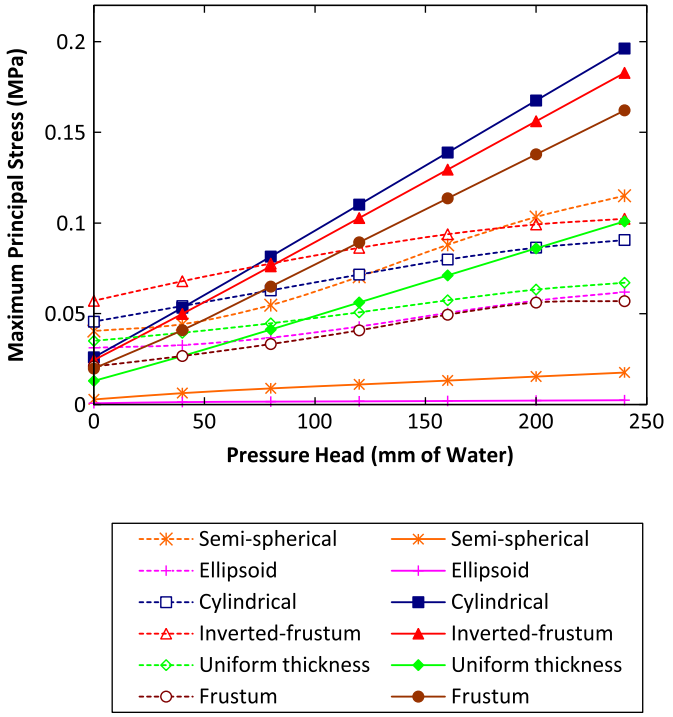

Fig. 13. Variation of the maximum principal stress on the "lip edge" (dash lines) and "bottom edge" (solid lines) of the filter models as the pressure head of water changes.

4.6. Implications

The implications of the current work are quite significant. First, the result shows clearly that the mechanical properties of porous ceramics are not a simple function of its density but depends largely on porosity, except for modulus and hardness which were more or less a function of the average pore size. Other possible factors that affect the mechanical strength of porous ceramics include: surface and internal defects (such as cracks) during processing (thermal shock), transportation (mechanical vibration) and usage (hydrostatic force). One way of solving this problem is to fabricate CWFs from homogeneous mixtures of clay and sawdust.

Future work should include research on porous ceramic structures that can offer greater resistance to crack growth during transportation, usage and processing. One way of improving the mechanical properties of the filter is to optimize the porous

structure of the filters [29]. Future ceramic water filters should also be made such that they have uniform thicknesses. Furthermore, if they are to be fabricated into "curvy" shapes, they have to be "as ellipsoidal as possible". Also, the receptacle has to span the entire lip of the filter and be as close to the side of the filter as possible. Future work is also needed to study the effects of doping and the effects of hydration on the structure and mechanical properties of porous clay ceramics. These are clearly some challenges for future work.

5. Conclusions

The porosity of clay ceramics increases with increasing volume fraction of sawdust. The higher skeletal density of HP reveals that the porous material has pore sizes that are smaller than what MP is capable of detecting. The modulus and hardness are functions of the average pore size. The strengths (compressive and flexural) and fracture toughness decreases with increasing porosity. The porous clay ceramic materials exhibit resistance-curve behavior that is typical of brittle materials, with limited crack growth resistance attributed to shielding by crack bridging. The shielding due to crack bridging can be predicted using a combination of SSB and LSB models. The wider the support provided by the receptacle, and the closer it is to the side of the filter, the better. Also, the more uniformly thick a filter is the better. Finally, if a filter has to be fabricated to be "curvy", the more ellipsoidal it is the better.

Acknowledgments

This work was supported by grants from the National Science Foundation (DMR 0231418) and The Grand Challenges Program at Princeton University. The authors would also like to thank Mr. Gerald Poirier and Professor George Scherer for useful technical discussions.

Appendix A. Supporting information

Supplementary data associated with this article can be found in the online version at http://dx.doi.org/10.1016/j.msea.2012.07.038.

References

[1] P. Colombo, Philos. Trans. R. Soc. A 364 (2006) 109–124.
[2] H.C. Vanderhorst, J.H. Hanemaaijer, Desalination 77 (1990) 235–258.
[3] D.J. Green, R. Colombo, MRS Bull. 28 (2003) 296–300.
[4] T. Clasen, W.P. Schmidt, T. Rabie, I. Roberts, S. Cairncross, Br. Med. J. 334 (2007) 782–785.
[5] M.D. Sobsey, C.E. Stauber, L.M. Casanova, J.M. Brown, M.A. Elliott, Environ. Sci. Technol. 42 (2008) 4261–4267.
[6] J. Brown, M.D. Sobsey, J. Water Health 8 (2010) 1–10.
[7] I. Yakub, W.O. Soboyejo, J. Appl. Phys. 111 (2012) 1243241–1243249, http://dx.doi.org/10.1063/1.4722326.
[8] WHO/UNICEF, Progress on Drinking Water and Sanitation: Special Focus on Sanitation, World Health Organization and United Nations Children's Fund Joint Monitoring Programme for Water Supply and Sanitation, Geneva, Switzerland, 2008.
[9] K.C. Friedman, in: Chemical and Biological Engineering, Princeton University, Princeton, NJ, 2010.
[10] T. Clasen, G.G. Parra, S. Boisson, S. Collin, Am. J. Trop. Med. Hyg. 73 (2005) 790–795.
[11] WHO, Guidelines for Drinking-Water Quality, 4 ed., Geneva, Switzerland, 2011.
[12] I. Yakub, A. Plappally, M. Leftwich, K. Malatesta, K.C. Friedman, S. Obwoya, F. Nyongesa, A.H. Maiga, A.B.O. Soboyejo, W.O. Soboyejo, J. Environ. Eng., in preparation.
[13] C.S. Low, in, Massachusetts Institute of Technology, 2002, pp. 147, leaves.
[14] R.W. Dies, in, Massachusetts Institute of Technology, 2003, pp. 170.
[15] I. Yakub, W.O. Soboyejo, J. Environ. Eng., in preparation.
[16] I. Yakub, in: Mechanical and Aerospace Engineering, Princeton University, Princeton, 2012.
[17] J. Brown, M.D. Sobsey, Environ. Technol. 30 (2009) 379–391.
[18] N.H. Tsao, in: Chemical and Biological Engineering, Princeton University, Princeton, NJ, 2011.
[19] V. Dupres, F.D. Menozzi, C. Locht, B.H. Clare, N.L. Abbott, S. Cuenot, C. Bompard, D. Raze, Y.F. Dufrene, Nat. Methods 2 (2005) 515–520.
[20] J.R. Morones, J.L. Elechiguerra, A. Camacho, K. Holt, J.B. Kouri, J.T. Ramirez, M.J. Yacaman, Nanotechnology 16 (2005) 2346–2353.
[21] W.D. Kingery, H.K. Bowen, D.R. Uhlmann, Introduction to Ceramics, 2nd ed., Wiley, New York, 1976.
[22] M. Saadaoui, G. Orange, C. Olagnon, G. Fantozzi, J. Mater. Sci. Lett. 10 (1991) 1090–1092.
[23] ASTME, ASTME 399-90: Standard Test Method for Plane Fracture Toughness of Metallic Materials, Philadelphia, 1990.
[24] T. Fett, Stress Intensity Factors, T-Stresses, Weight Functions, IKM 50, Universitätsverlag Karlsruhe, Karlsruhe, 2008.
[25] T.J. Baker, J. Zimba, E.T. Akpan, I. Bashir, C.T. Watola, W.O. Soboyejo, Acta Mater. 54 (2006) 2665–2675.
[26] J. Lou, K. Bhalerao, A.B.O. Soboyejo, W.O. Soboyejo, Cement Concrete Compos. 25 (2003) 599–605.
[27] T. Fett, D. Munz, Stress Intensity Factors and Weight Functions, Computational Mechanics Publications, Southampton, UK, Boston, Mass. USA, 1997.
[28] M. Bellotto, A. Gualtieri, G. Artioli, S.M. Clark, Phys. Chem. Miner. 22 (1995) 207–214.
[29] Z.Y. Deng, T. Fukasawa, M. Ando, G.J. Zhang, T. Ohji, J. Am. Ceram. Soc. 84 (2001) 2638–2644.
[30] F.P. Knudsen, J. Am. Ceram. Soc. 42 (1959) 376–387.
[31] R.W. Rice, J. Mater. Sci. 31 (1996) 1969–1983.
[32] R.W. Rice, Key Eng. Mater. 115 (1996) 1–19.
[33] A.S. Wagh, R.B. Poeppel, J.P. Singh, J. Mater. Sci. 26 (1991) 3862–3868.
[34] D.M. Liu, Ceram. Int. 23 (1997) 135–139.
[35] A.R. Boccaccini, J. Mater. Sci. Lett. 17 (1998) 1273–1275.
[36] P. Duran, J.F. Fernndez, On the Porosity Dependence of the Fracture Strength of Ceramics, in: A.R. Boccaccini, G. Ondracek (Eds.), Faenza Editrice Iberica S.L., Madrid, 1993, pp. 895–900.
[37] R.W. Rice, J. Mater. Sci. 28 (1993) 2187–2190.